IEEE Access
Multidisciplinary | Rapid Review | Open Access Journal

Received March 2, 2019, accepted March 22, 2019, date of publication March 27, 2019, date of current version April 16, 2019.

Digital Object Identifier 10.1109/ACCESS.2019.2907735

Ammunition Reliability Against the Harsh Environments During the Launch of an Electromagnetic Gun: A Review

HE ZHANG, KEREN DAI, AND QIANG YIN

ZNDY of Ministerial Key Laboratory, School of Mechanical Engineering, Nanjing University of Science and Technology, Nanjing 210094, China

Corresponding authors: He Zhang (hezhangz@njust.edu.cn) and Keren Dai (dkr@njust.edu.cn)

This work was supported in part by the National Natural Science Foundation of China under Grant 61403201, in part by the Six Talent Peak Projects under Grant KTHY-019, and in part by the Key Basic Research Projects of Basic Strengthening Plan under Grant 2017-JCJQ-ZD-004.

ABSTRACT Electromagnetic railguns have an advantage over traditional chemical propulsion weapons, in that the projectile can be accelerated to extremely high speeds and effective damage can be achieved. However, during the launch from an electromagnetic railgun, the ammunition will be subject to a harsh environment, including very strong and violently changing electromagnetic fields, high-*g* acceleration impact, high temperatures, and so on; and thus, the reliability of the fuze is threatened, and the safety and damage effectiveness of the ammunition will be seriously degraded. In this paper, the harsh environment during the launch process is first reviewed, including the experimental data, the modeling, and simulation of the multiphysics fields. In particular, the coupling effect of these multiphysics fields are revealed, which aggravates the extreme environment. Furthermore, this paper reviews the protection of fuzes against strong magnetic fields and high-*g* impacts from three aspects, namely, materials, devices, and systems, and presents prospects for future research. This review will guide studies on the protection of fuzes and the stability of ammunition, as well as promote the effectiveness of electromagnetic railguns.

INDEX TERMS Electromagnetic launching, fuze, reliability, harsh environment of multiphysics fields, electromagnetic shielding, anti-high-*g* impact technology.

I. INTRODUCTION

To enhance the performance of conventional artillery in future high-tech battlefields, such as for protective armor destruction, air defense and destroying missiles, the speed of the projectile must be greatly increased to achieve ultrahigh kinetic energy. However, due to the stagnation speed of gunpowder gas, the initial velocity of traditional chemical propulsion weapons can hardly exceed 2 km/s [1]. Under this circumstance, a new concept of launch technology emerged: the electromagnetic launch technology. This technology converts electromagnetic energy into mechanical kinetic energy and utilizes the electromagnetic force to accelerate the payload, such as shells, missiles, rockets and even airplanes, to an ultrahigh velocity within an extremely short start-up period of time [2]. Among the various electromagnetic launch technologies, the electromagnetic railgun technology [3]–[5] is the one that is most likely to find practical applications, and its development is the most mature.

The associate editor coordinating the review of this manuscript and approving it for publication was Cristian Zambelli.

The mechanism of the electromagnetic railgun was first verified in 1944 [6]. With the advancements in large power supplies over the past few decades, the muzzle velocity of the projectile has been greatly increased, and the equipment has gradually become mature for practical applications [7]–[10]. The power of the power supply designed by [11] reaches 10 MJ, and the energy density of the power supply designed in the study [12] reaches 500 kJ/m^3, basically satisfying the energy supply requirements of the electromagnetic railgun. In terms of weapons applications, in 1978, the US Department of Defense established a national advisory committee and technical department for evaluating electromagnetic railgun research. The Armaments, Research, Development, and Engineering Center (ARDEC) and the Defense Advanced Research Projects Agency (DARPA) have become the main sponsor for research on electromagnetic railgun technology by research institutions [13], and research on electromagnetic railguns has continuously achieved new results [14]–[25]. In December 2010, the US Navy conducted a launch at the Naval Surface Warfare Center, Dahlgren Division

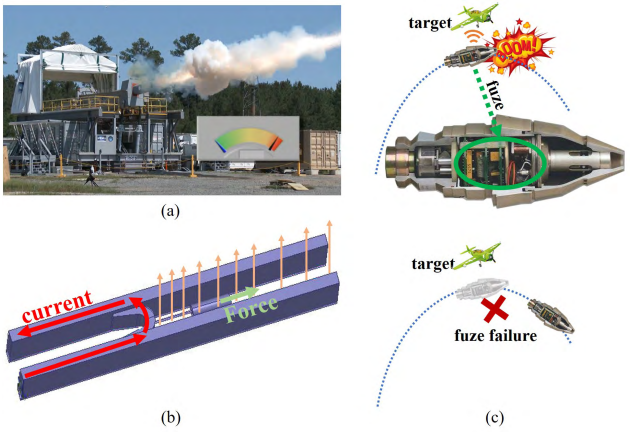

FIGURE 1. (a) The instant of launch from the video. (b) Schematic diagram of the key components of an electromagnetic railgun [36]. (c) Control of ammunition detonation by the proximity fuze.

(NSWCDD) [24], [25], where they successfully accelerated the projectile to an initial velocity of 2500 m/s with a muzzle kinetic energy of 33 MJ [26]. In July 2017, the US Navy conducted the first continuous burst test of electromagnetic railguns at NSWCDD, where they successfully launched two projectile in 25 seconds at a speed of 2 km/s [27]. The instant of launch from the video is shown in Fig. 1(a).

An intelligent fuze controls the detonation of the ammunition and plays an important role in ensuring its effectiveness. On the one hand, intelligent fuzes can perceive the surrounding environment such that the safety of the ammunition can be ensured and accidental explosions can be prevented [28]. On the other hand, intelligent fuzes can also recognize the intended target such that the accuracy of the ammunition explosion can be ensured and the damage effect can be maximized [29], [30]. Taking the proximity fuze as an example, as shown in Fig. 1(c), the fuze detects the target by emitting and receiving electromagnetic waves, and it detonates when the target distance is close enough. If the fuze fails, the ammunition will fly over the target without exploding and will not be able to effectively damage the intended target.

A series of tests on fuzes in harsh environments during launch have been conducted, but unfortunately, various failures of the fuze have been found [31], [32]. The reliability of fuzes during the launch becomes a bottleneck in the research of electromagnetic railguns. As shown in Fig. 1(b), during the launch, the driving force of the projectile comes from the strong and violently changing electromagnetic field, and the projectile is quickly accelerated to an ultrahigh velocity in an extremely short period of time, leading to a high-g impact. Moreover, Joule heating and friction heating are unavoidable. As the acceleration time of the electromagnetic railgun becomes increasingly shorter and the initial velocity becomes increasingly higher, the extreme environment inside the bore becomes increasingly more extreme [33]–[35]. Therefore, to ensure the damage effectiveness of the ammunition, research on the safety and reliability of the fuze is of great significance.

To improve the reliability of the fuze and to promote the practical applications of electromagnetic railguns, recent studies have focused on the following key problems. First, it is difficult to measure the harsh environment during the launch. Therefore, accurate modeling and simulation must be conducted to guide the design for fuze protection. Second, the harsh environment during the launch involves the coupling effect of multiphysics fields, making the model and simulation extremely complicated. Finally, the protection of the key devices and systems depends only on one isolated means, which is not sufficient and needs to be strengthened. This paper provides a comprehensive review and discussion of recent research on these key issues, and it presents prospects for future research.

II. HARSH ENVIRONMENT IN THE LAUNCH PROCESS

During the launch of an electromagnetic railgun, the magnetic field is extremely strong and varies violently. The projectile is accelerated to an ultrahigh velocity within an extremely short period of time, leading to a high-g impact. Moreover, the friction and Joule heating effect cause a high temperature. Quantitative research on the strong magnetic field, the high-g impact and the high temperature must be conducted to guide the protection of electromagnetic railguns. In this section, studies on measurements based on experiments and on modeling and simulations are presented.

A. STRONG MAGNETIC FIELD

1) EXPERIMENTAL RESULTS

During the launch of an electromagnetic railgun, a strong magnetic field, as large as more than 1 T or even tens of T, will be generated. The electromagnetic field changes drastically with time, taking only a few milliseconds from generation to disappearance. Moreover, the magnetic field is unevenly distributed in space, decreasing rapidly from the armature toward the muzzle. Therefore, measuring such a strong and changing magnetic field is difficult and has long been problematic for researchers. In recent years, with the application of colossal magnetoresistance-B-scalar (CMR-B-scalar) sensors, the measurement of the strong and changing magnetic field environment has been greatly improved [37], [38].

In [38], a measurement system based on CMR-B-scalar sensors is studied. The output of the CMR sensor is processed by the B-scalar meter such that a precise measurement of the magnetic field is achieved. A diagram of the key components of the system is shown in Fig. 2a. To ensure the measurement accuracy on the strong magnetic field, a special design for the B-scalar meter is implemented. First, a metal shielding structure is applied to ensure normal operation of the electronics in the measurement systems (e.g., the digital signal processing (DSP) chips). Second, the minimum number of analog devices is applied in the design, and the output from the CMR sensor is converted to the measurement of the magnetic field through DSP.

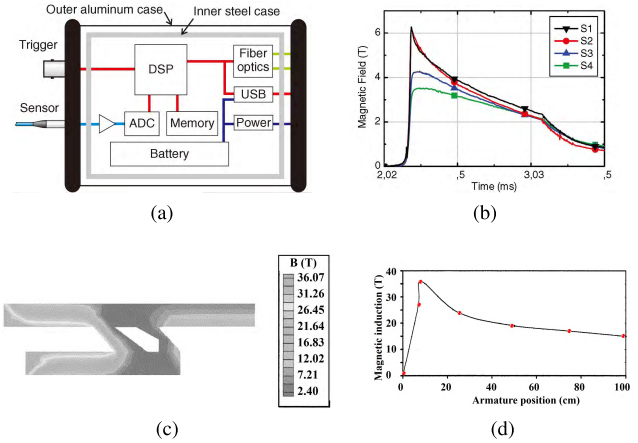

FIGURE 2. (a) Key functional blocks of the B-scalar meter [38]; (b) magnetic field measurements performed using the B-scalar measurement system during a railgun shot [38]; (c) magnetic induction control for the rail and the armature at 1 cm position [39]; (d) magnetic induction control for the rail and the armature at different positions [39].

Based on this measurement system, the magnetic environment during a single launch is tested with the railgun named RAFIRA (rapid fire railgun)) [40], as shown in Fig. 2b. The magnetic field between the rails is measured by sensor S1, and the magnetic field every millimeter from the surface of the rail is measured by sensors S2-S4. It takes less than 0.1 ms for the magnetic field to increase to more than 3 T during a single launch of the railgun, and the magnetic field distributes unevenly in space. Under such a large magnetic field strength, the reliability of the fuzes is doubtful and worthy of further study. However, the magnetic field strength changes greatly with time and space; thus, it is difficult to obtain a complete and accurate magnetic field distribution through experimental measurements. To guide the design of the electromagnetic protection for the fuze, it is necessary to study the magnetic field through modeling and simulations.

2) MODELING AND SIMULATIONS

The geometry of the electromagnetic rails and armature is shown in Fig. 1(b). Due to the symmetry, the magnetic field in the upper part of the rails and armature is considered in the simulation. The electromagnetic launch process is achieved based on the driving force on the armature generated by the alternating electric and magnetic fields. In the traditional model [39], only the interaction of electric and magnetic fields governed by Maxwell's equations is considered,

$$\nabla \times \vec{B} = \mu \cdot \vec{J} \tag{1}$$

$$\nabla \times \vec{E} = -\frac{\partial B}{\partial t} \tag{2}$$

$$\vec{J} = \sigma \cdot \left(\vec{E} + \vec{V} \times \vec{B}\right) \tag{3}$$

where B is the magnetic induction field, μ is the magnetic permeability, J is the current density, E is the electric field intensity, and V is the material velocity.

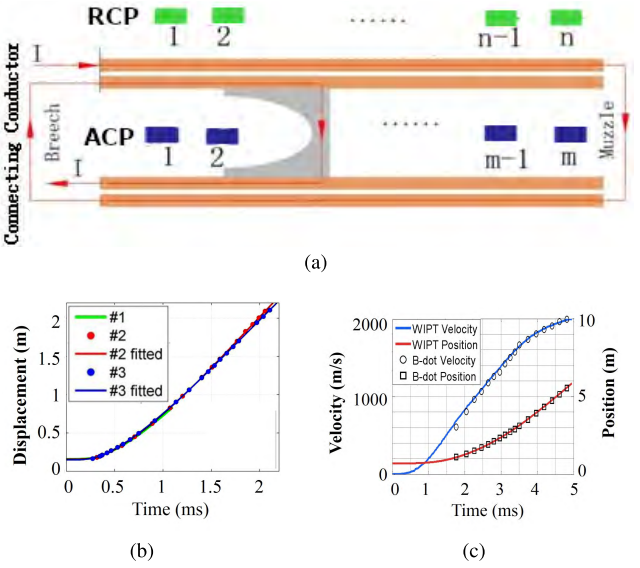

FIGURE 3. (a) Schematic of a series-augmented railgun and B-dot arrays [41]; (b) measured and fitted position versus time by VISAR (#1), ACPs (#2), and RCPs (#3) [41]; (c) comparison of in-bore WIPT velocity (blue) and calculated position (red) to the recorded B-dot sensor data [42].

According to this model, a simulation of the magnetic field distribution of the rails and armature is shown in Fig. 2c. When the armature is at different positions, the maximum magnetic field strength is as shown in Fig. 2d. With the motion of the armature, the magnetic field strength first increases sharply and then decreases slowly, and the maximum strength reaches 36 T.

These modeling and simulation studies provide a basic tool for theoretically analyzing the magnetic field during the launch process, partially replacing extensive repeated experiments. However, for model simplification and computational complexity reduction, the coupling of electromagnetic fields with mechanics and armature motion is neglected, which will be discussed in depth in Section III.

B. HIGH-G IMPACT

1) EXPERIMENTAL RESULTS

Since the launch process is extremely short, less than 10 ms, and the velocity of the projectile at the muzzle can be up to 2000 m/s, the acceleration can be greater than 200,000 m/s^2. Traditionally, indirect measurements such as B-dot measurements [41] are applied for velocity or acceleration. A diagram of the B-dot measurement system is shown in Fig. 3a. Armature current probes (ACPs) and rail current probes (RCPs) are placed along the axis of armature motion and the rail, respectively. For ACPs, the measured current peak only appears at the moment the armature passes its position; for RCPs, the measured current is near 0 before the armature passes, and it becomes a large and stable value after the armature passes. Therefore, the moment when the current changes the most sharply is the moment when the armature passes its position. Thus, the moment when the armature passes through these probes can be estimated; furthermore,

the velocity and acceleration of the armature over time can be inferred.

During the launch process, the projectile is fixed to the armature via the sabot. Although the movement of the armature with the projectile is slightly different from that of the individual armature due to the increase in mass, for the convenience of research, the motion of the projectile is usually approximated by that of the individual armature, which is presented in [41] and other literatures.

Based on the B-dot measurement system in [41], the position of the armature during a single launch is shown in Fig. 3b. The launch is repeated three times, and the positions are measured by the laser Velocity Interferometer System for Any Reflector (VISAR) (#1), ACPs (#2), and RCPs (#3), respectively. The consistency of the results measured with different measurement systems in three independent launch processes indicates that they can all be applied to measure the displacement and velocity during the launch of the electromagnetic railgun. However, they all have shortcomings. For ACPs (#2) and RCPs (#3), the measurement is difficult to perform at the initial stage of the railgun launch, i.e., 0-0.2 ms, and it can only be estimated by data fitting. In particular, the moment when the armature starts to move is difficult to determine. VISAR (#1) provides more accurate position and velocity measurements at the beginning of the launch process, but its measurement accuracy relies on a very precise setup and calibration, which is susceptible to interference in practical applications, particularly in the case of high-speed motion.

To achieve an accurate measurement of the entire process of an electromagnetic railgun launch, a new W-band In-bore Projectile Tracking WIPT) radar is studied in [42], and the measured velocity of the projectile during the launch is shown in Fig. 3c. It realizes precise measurements of the entire launch process, from low velocity near 0 to high velocity up to 2500 m/s. The assembly of the components is relatively simple, and the requirements for environmental conditions are relatively relaxed. The detection signal chain contains a DC component, which makes the velocity of the projectile directly related to the observed frequency of the echoes.

$$V = f_O \frac{c}{2f_E} \tag{4}$$

where f_O is the Doppler frequency shift, c is the speed of light, and f_E is the frequency of the transmitted detection signal, which is 94 GHz.

The above measurement results indicate that during the launch process of an electromagnetic railgun, the acceleration is extremely large, with an average acceleration of approximately 7×10^4 g and a maximum of 1.2×10^5 g. In this case, the electronic components of the fuze are prone to failure due to the high-g impact. Therefore, it is of great significance to conduct modeling research on the acceleration impact during the launch process to guide the design for protection of the fuze.

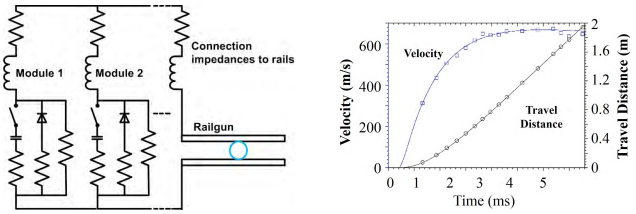

FIGURE 4. (a) Circuit model of the PFN (pulse forming network) and railgun [43]; (b) velocity and travel distance of shot #01. Data points are from measurement by B-dot probes, and the lines are from circuit calculation [43].

2) MODELING AND SIMULATION

Since the acceleration is derived from the velocity of the armature, the modeling and simulation are also based on the motion of the armature. The launch process of the electromagnetic railgun will have a complex effect on the magnetic field, while the change of the magnetic field will in turn affect the movement process of the armature. Due to this coupled effect, the motion of the armature becomes very complicated. To reduce the computational complexity, Equivalent circuit model was applied in early research [43], as shown in Fig. 4a.

The circuit equation changes dynamically with the motion of the armature, while the change of the circuit equation in turn affects the motion of the armature. Suppose that there is a linear relationship between the inductance of the rail and the length, as well as the resistance of the rail and the length; mark these gradients as L' and R', respectively. Thus, the breech voltage is

$$U_b = L'(x + x_0)\frac{dI}{dt} + L'\frac{dx}{dt}I + R'(x + x_0)I \tag{5}$$

where x and x_0 are the moving position and the initial position of the armature from the breech end, and I is the rail current.

The circuit can be modeled with coupled second-order differential equations,

$$[M]\ddot{U} + [D]\dot{U} + [K]U = \{0\} \tag{6}$$

where $\{U\}$ is the vector of capacitor voltages and $[M]$, $[D]$, and $[K]$ include all the electrical impedance parameters of the pulse forming network and railgun.

The equation of motion of the armature is

$$m\frac{d^2x}{dt^2} = F_p - 2\mu\left(F_{N,me} + F_{N,em}\right) \tag{7}$$

where m is the armature mass, μ is the friction coefficient, F_p is the electromagnetic propulsion force of the armature, $F_{N,me} = 3800$ N is the mechanical normal force, and $F_{N,em}$ is the electromagnetic normal force. There is,

$$F_p = \tfrac{1}{2}L'I^2 \tag{8}$$

$$F_{N,em} = \alpha F_p \tag{9}$$

With this model, the motion process of the armature is simulated in [43], and the results are compared with the B-dot measurement, as shown in Fig. 4b, where the data points are

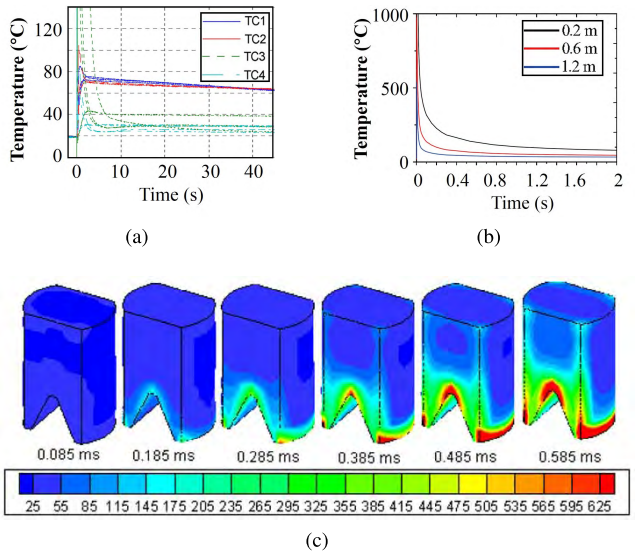

FIGURE 5. (a) Raw thermocouple data on UNS C18200 [33]; (b) time-varying curves for three-point temperature on rail surface. [44]; (c) evolution of armature temperature (°C) [45].

from measurements by B-dot probes, and the lines are from simulation of circuit model. Although the simulation results agree well with the measured data, in fact, the accuracy of this model depends on the parameters, which need to be determined through complex experiments. Therefore, compared with the multiphysics model, the equivalent circuit model has inherent shortcomings. In Section III, the coupling effect between high-g impact and magnetic field, electric field, and temperature field will be discussed in depth based on the multiphysics model.

C. HIGH TEMPERATURE

1) EXPERIMENTAL RESULTS

During the launch of an electromagnetic railgun, a large amount of heat is generated due to the large current and high-speed friction. In [33], 4 sets of thermocouples (TC1-TC4) are arranged along the rail of negative polarity, and each set is composed of 3 or 4 thermocouples that are close to each other. The temperature measured by each thermocouple during a single launch is shown in Fig. 5a. When the launch starts, the temperature of the rail sharply increases, exceeding 140°C. The temperature at different positions (different TC set) varies greatly, as well as even within one TC set, meaning that at a very close distance, there is also a significant difference in temperature. Therefore, it is very difficult to study the temperature distribution inside the bore during the launch through experimental tests, and research through modeling and simulation of the temperature change is a must.

To make matters worse, the heat dissipation process after the launch is very slow. After 1 minute, the temperature of the two groups of thermocouples closer to the breech block, which are TC1 and TC2, still exceeds 60°C. In practical applications, it is necessary to complete multiple launches per minute; thus, the heat inside the bore will accumulate continuously, and the temperature will be several times higher than that of a single launch. Consequently, it poses a much more serious threat to the normal operation of the rails and electronic devices of the fuzes. Moreover, the frequency of continuous launch of the electromagnetic railgun is limited, seriously affecting its actual combat performance.

2) MODELING AND SIMULATION

Since the launch of the magnetic railgun is an extremely short process, the generated heat will be considerably larger than the heat dissipation to the surroundings and will definitely cause a sudden increase in temperature. Early researchers [44] studied the temperature distribution through an equivalent circuit model similar to Fig. 4a. The heat generated during the launch of the electromagnetic railgun is composed of two parts, Joule heat P_r and friction heat P_f,

$$\begin{aligned} P &= P_r + P_f \\ &= I^2 R_c + \mu(F_0 + F_m)v \end{aligned} \tag{10}$$

$$F_m = \frac{L}{2I^2}\cos\alpha \tag{11}$$

where I is the driving current, R_c is the contact resistance during armature launch, v is the armature velocity, μ is the coefficient of sliding friction, F_0 is the preloaded force of the armature, F_m is the electromagnetic pressing force generated from the two arms of the C-shaped armature, and α is the intersection angle between the arms of the armature and the rails.

From t_1 to t_2, the armature moves from $x(t_1)$ to $x(t_2)$, and the average heat flux in this region is

$$\bar{E} = \frac{\lambda \int_{t_1}^{t_2} P(t)dt}{h(t_2 - t_1)\int_{t_1}^{t_2} v(t)dt} \tag{12}$$

where λ is the proportion of heat conducted into the rails in friction heat totally generated in the interface and h is the bore height.

According to this model, the temperature distribution on the surface of the rail changing with time is as shown in Fig. 5b [44]. The temperature at all positions inside the bore sharply increases at the moment of launch, exceeding 500°C, but then slowly decreases. However, the parameters of this equivalent circuit model also depend on complex experimental measurements, and the coincidence between the simulation results [44] and the experimental tests [33] is significantly different. That is, although the model is simple to calculate, accurate simulation can hardly be achieved.

To reveal the temperature change of the armature at the moment of the launch more accurately, a physics field-based model is studied in [39], [45]. Considering the fact that temperature at any position is affected by the thermal diffusion and the heat generation at the same time,

$$\nabla \cdot (k\nabla T) + S = \rho C \frac{dT}{dt} \tag{13}$$

where T is the temperature, C is the specific heat, ρ is the density, k is the thermal conductivity, and S is the source of

heat, including the Joule heat S_{ohm}, the friction heat $S_{friction}$ and the latent heat S_{latent},

$$S = S_{ohm} + S_{friction} + S_{latent} = \frac{\vec{J} \cdot \vec{J}}{\sigma} + \mu_k F_c V - \rho L F(T) \frac{\partial T}{\partial t} \quad (14)$$

where μ_k is the friction coefficient, F_c is the contact force (at the interface), L is latent heat, and $F(T)$ is referred to [46].

Combining the above model with the model of the magnetic field in Section II-A, a simulation is conducted [45]. The temperature distribution inside the bore, particularly on the surface of the armature, is shown in Fig. 5c. During the launch process, the temperature of the armature increases sharply, and its distribution is uneven, especially concentrated at the tail. Based on this model, the temperature of the armature during the launch is presented, providing a basis for studying the coupling effect of multiphysics fields.

D. LIMITATIONS OF MODELING ON SINGLE FIELD

A large number of experimental tests, modelings and simulations have been conducted on the characteristics and formation mechanism of the harsh environment, including strong magnetic field, high-g impact, and high temperature, during the launch of an electromagnetic railgun. In the next section, we will review the coupling effects between these extreme factors and describe their formation mechanisms more thoroughly.

III. THE 'CHAIN REACTION': THE DECISIVE ROLE OF MULTIPHYSICS COUPLING ON EXTREME ENVIRONMENTS

In fact, among the extreme factors, i.e., the strong magnetic field, high-g impact and high temperature, a dynamic change of one factor has a profound influence on the other two factors. For example, the motion of the armature changes the spatial distribution of the drive current, thereby affecting the spatial distribution of the magnetic field and the generation of Joule heat.

The coupling effect among such multiple physical fields often leads to a 'chain reaction' of the dynamics processes of multiphysics fields. Consequently, it is extremely easy to run out of control in a very short period of time, forming an extremely harsh environment. One of the typical representatives of the runaway effect under the multiphysics coupling effect is the thermal runaway process of lithium batteries [47]. On the one hand, the electrochemical reaction generates heat and increases the temperature. On the other hand, the high temperature promotes the electrochemical reaction. Consequently, a 'chain reaction' is formed, increasing the temperature of a lithium battery by hundreds of degrees in a very short time and causing disastrous consequences. Similarly, during the launch of an electromagnetic railgun, the coupling effect between the electromagnetic field, armature motion and temperature distribution will also lead to a 'chain reaction' and exacerbate the harsh environment. Therefore, multiphysics modeling must be performed for accurate simulations and design guidance.

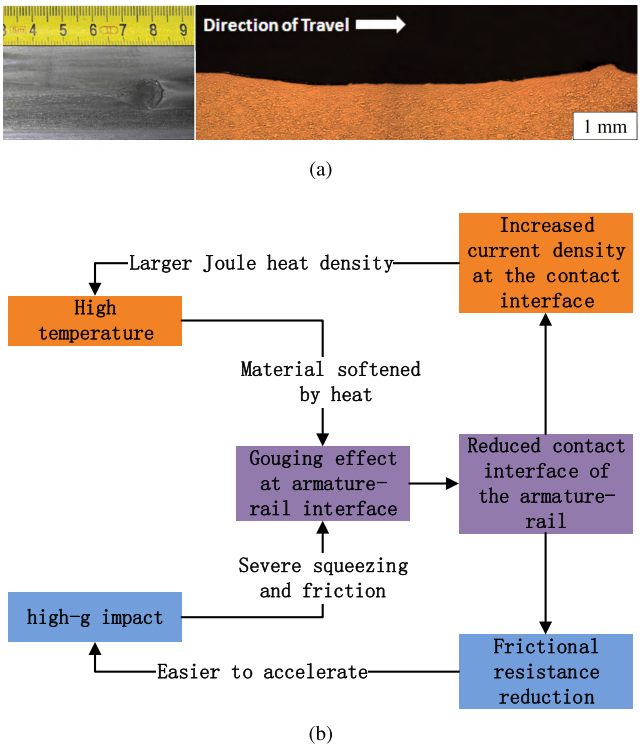

FIGURE 6. (a) Typical teardrop-shaped gouge crater and its microscopic view in railgun experiment [48] [49]; (b) a diagram of the gouging effect.

A. THE COUPLED MECHANICAL-TEMPERATURE FIELDS: THE GOUGING EFFECT

In the early research of electromagnetic railguns, it was ideally assumed that the geometry and material characteristics of the armature and the rails remained unchanged during the launch. However, many experiments have verified that there is in fact a significant gouging effect at the contact interface between the rails and the armature during the launch, that is, the material at the contact interface melts at high temperatures [48], [49]. A teardrop-shaped gouge crater and its microscopic view in the railgun experiment are shown in Fig. 6a.

The gouging effect causes accumulated damage to the rails and armature of the electromagnetic railgun, affecting the accuracy of the subsequent launch. Moreover, the gouging effect is coupled with the effect of high-g impact and high temperature, leading the extreme environment during the launch to a more extreme level. The mutual relationship between the mechanical field, the temperature field and the gouging effect is shown in Fig. 6b. On the one hand, the temperature increase causes the rail and the armature to be softened by heat, and the high-g impact causes the rail and the armature to be more severely squeezed and rubbed. The combination of these two effects leads to a gouge at the interface of the armature and rails, and the area of the contact interface is further reduced. On the other hand, the reduction in the

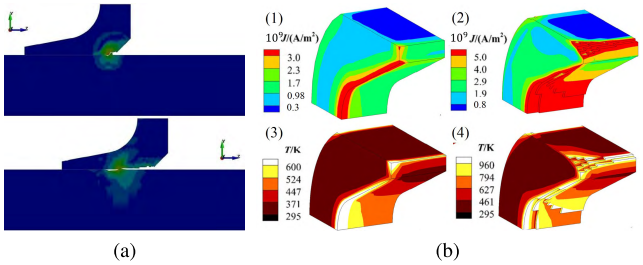

FIGURE 7. (a) Mises stress during gouge formation process. [48]. (b) Current density and temperature of the armature: (1) current density at t = 0.2 ms; (2) current density at t = 1.0 ms; (3) temperature at t = 0.2 ms; (4) temperature at t = 1.0 ms [51].

contact interface leads to an increase in the current density on the contact interface, resulting in a larger Joule heat density and a further increase in the temperature. A reduction in the contact interface also leads to a reduction in the frictional resistance. Thereby, the acceleration process of the armature is more intense, and the impact is further enhanced. A further enhancement of high temperature and high-g impacts will exacerbate the gouging effects, and their interactions form a 'chain-reaction' that makes the extreme environment more extreme in a very short time.

A model of the gouging effect during the launch is established in [48]. Fracture occurs when the accumulated effective plastic strain reaches the strain at fracture, which is

$$D = \sum \frac{\Delta \bar{\varepsilon}^p}{\varepsilon^f} \geq 1 \tag{15}$$

where $\bar{\varepsilon}^p$ is the effective plastic strain and ε^f is the strain at fracture.

According to the Johnson-Cook model [50], $\bar{\varepsilon}^p$ is decided by the stress along the y axis,

$$\sigma_y = [A + B(\bar{\varepsilon}^p)^n](1 + c \ln \varepsilon^*)(1 - T^{*m}) \tag{16}$$

$$T^* = \frac{T - T_{room}}{T_{melt} - T_{room}} \tag{17}$$

where A, B, n, c, and m are input constants; ε^* is the normalized effective plastic strain rate; T_{melt} is the melting temperature of the materials; and T_{room} is the temperature of the environment.

The strain at fracture is expressed as

$$\varepsilon^f = \left(D_1 + D_2 e^{D_3 \sigma^*}\right)(1 + D_4 \ln \varepsilon^*)(1 + D_5 T^*) \tag{18}$$

where $\sigma^* = p/\sigma_{eff}$ is the ratio of pressure divided by the effective stress; D_1, D_2, D_3, D_4, and D_5 are failure parameters; and p is the pressure associated with the material.

According to the above model, a simulation of the strain distribution of the rails and armature at different times is shown in Fig. 7a. As the launch process progresses, the strain on the rails and armature becomes large. From the point of maximum stress, the gouge crater gradually occurs and spreads to the root, resulting in a decreasing contact area between the armature and the rails.

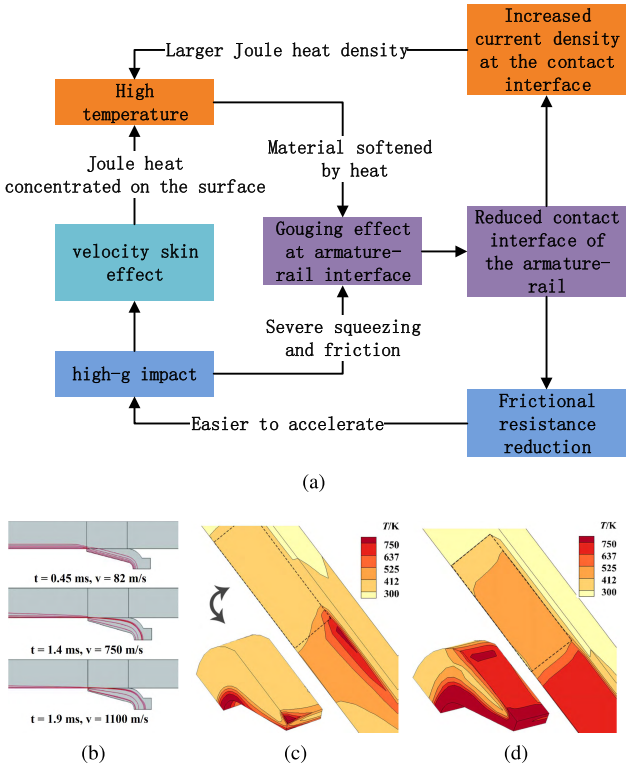

FIGURE 8. (a) Diagram of the gouging effect with the velocity skin effect; (b) evolution of current density at different time steps [52]; (c) temperature at low velocity [53]; (d) temperature at high velocity [53].

The significant effects of the agglomeration of current density and rapid increase in temperature during the gouging process are studied through a finite element simulation [51]. The distributions of current density and temperature at 0.2 ms and 1.0 ms after launch are shown in Fig. 7b. Comparing Fig. 7b(1) and (2), as the launch progresses, the contact interface between the armature and the rails is gouged, and the contact area is reduced, resulting in a rapid increase in the current density of the remaining contact interface on the armature. Comparing Fig. 7b(3) and (4), the current density of the contact interface increases sharply due to the gouging effect, causing the Joule heating effect to concentrate on a smaller contact surface. Consequently, the temperature of the contact region sharply increases, and the maximum temperature increases from 600 K to over 960 K.

The experimental data validate the 'chain reaction' effect. Under the coupling effect of multiphysics fields, the harsh environment during the launch is indeed aggravated; thus, the study of the protection of fuzes during the launch is of greater significance.

B. STRENGTHENING OF THE GOUGING EFFECT DUE TO THE VELOCITY SKIN EFFECT

Furthermore, considering the coupling effect of the accelerated motion of the armature on the electromagnetic field during the launch process, the gouging effect will be further aggravated, as shown in Fig. 8a.

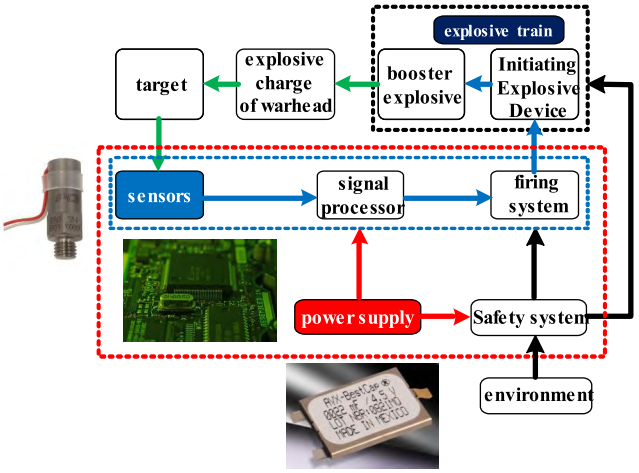

FIGURE 9. Key components and photos of the fuze.

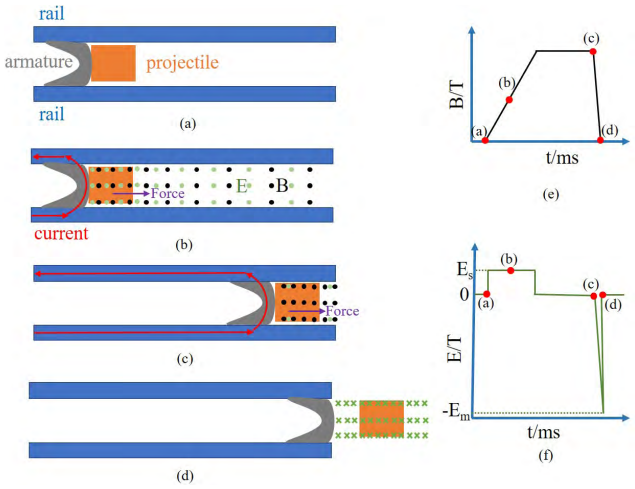

FIGURE 10. Schematic diagram of changes in the induced magnetic field and induced electric field during the launch process of an electromagnetic railgun. (a)-(d) Schematic diagram of the movement process of the armature and the changes of the magnetic field and electric field. (e) Induced magnetic field strength over time. (f) Induced electric field strength over time.

As the speed of the armature increases, the current distribution in the rail will result in a 'velocity skin effect' [45], [52], that is, current is concentrated on the surface of the rail, causing an extremely large current density, as shown in Fig. 8b. The 'velocity skin effect' will cause the Joule heat to be more concentrated and aggravate the heating of the interface of the rails and armature. Thus, it will take much less time for the gouging effect to be very seriously and even out of control.

A simulation of the temperature distribution of the armature at different speeds is conducted [53], as shown in Fig. 8c and Fig. 8d. When the initial velocity of the armature is increased, the temperatures on the armature and the rails are sharply increased to more than 700 K, and the temperature distribution is more concentrated on the surfaces and the armature-rail interface. To summarize, the velocity skin effect contributes to the concentration of heat in a local area, aggravating the gouging effect and resulting in a more extreme environment with multiphysics fields.

IV. PROTECTION OF THE KEY COMPONENTS OF FUZES IN HARSH ENVIRONMENTS

The fuze is the key to ammunition for environment detection and target recognition, ensuring the its safety and maximizing its damage effectiveness. As shown in Fig. 9, the fuze microsystem consists of sensors, power supply, processors, detonation actuator modules, and so on. These electronic devices are prone to temporary failure or even irreversible damage in the extreme environment during the launch of the electromagnetic railgun, causing the fuze to malfunction and affecting the damage performance of the ammunition. Therefore, protecting the key components of fuzes, especially the sensors, basic electronic devices and power supply, is of great importance.

The phenomenon and the formation mechanism of the strong magnetic field environment, strong mechanical impact environment and high temperature environment during the launch of an electromagnetic railgun have been discussed in detail in Section II and Section III. In fact, for most ammunition, the fuzes are placed in front of the missile, which is far away from the heat-generating position of the armature. Thus, during the very short launch process, it is almost unaffected by the armature and hard to produce a significant temperature increase. Therefore, the failure mechanism and protection method of electronic devices in the fuze under strong magnetic fields and strong mechanical impact are discussed in the following.

A. FAILURE OF THE FUZE IN STRONG MAGNETIC FIELD ENVIRONMENT

1) CHARACTERISTICS OF STRONG MAGNETIC FIELDS DURING THE LAUNCH

The strong magnetic field during the electromagnetic railgun launch changes dramatically. As measured in [37], the strength of the magnetic field can be roughly divided into three stages: rising stage, flat stage and decreasing stage. However, the magnetic field experienced by the fuze is not exactly the same as the magnetic field in the gun. The main difference is in the final stage, when the fuze is pushed out of the bore, and the magnetic field strength decreases in a very short time [54].

The magnetic field experienced by the fuze is summarized as follows. Before the launch, as shown in Fig. 10(a), the projectile is fixed to the armature at the rail of the bore. In the first stage, at the beginning of the launch process, as shown in Fig. 10(b), the current in the armature increases from 0 to a very large value, and thus, the induced magnetic field around the armature gradually increases. Therefore, the propulsion force increases until beyond the static friction force, and the projectile starts to move. The increasing magnetic field also results in an induced electric field in the same direction. In the second stage, as shown in Fig. 10(c), the projectile is

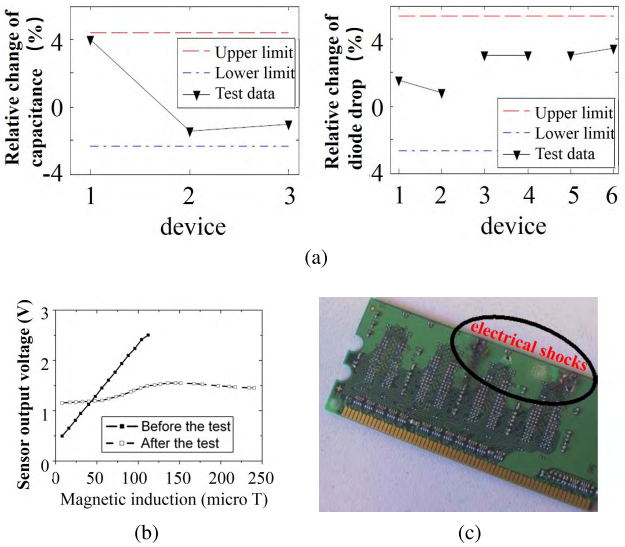

FIGURE 11. (a) The effect of static strong magnetic fields on the characteristics of basic components and semiconductor components [54]; (b) characterization curve of the single-axis fluxgate magnetometer before and after the static railgun test; (c) electrical shocks on DDR2-RAM module after the muzzle test [55].

accelerated inside the bore until reaching the muzzle, during which the current and magnetic field fluctuate slightly, and the induced electric field is also very weak. In the last stage, as shown in Fig. 10(d), when the projectile is pushed out of the muzzle, the magnetic field drops to 0 in a moment due to a magnetic-free environment outside the bore. Therefore, at this moment, a very strong induced electric field in the reverse direction will be generated, which will then disappear quickly due to the magnetic-free environment outside. Diagrams of the induced magnetic field strength and induced electric field strength changing with time are shown in Fig. 10(e) and Fig. 10(f), respectively.

2) FAILURE PHENOMENON

Among the three stages of the aforementioned electromagnetic railgun propulsion, the relatively stable phase of the magnetic field is the simplest one. Many researchers have studied this stage by testing the fixed electronic components in a constant strong magnetic field [54]. Under this situation, the researchers tested the performance of basic components such as resistors, capacitors, inductors, semiconductor components such as diodes and triodes, and more complex single-chip microcomputers under static strong magnetic fields, and they verified that there is no performance change for these components. Some of the test results are shown in Fig. 11a. Therefore, during the launch process of an electromagnetic railgun, it is necessary to focus on the influence of the alternating electromagnetic field during the initial stage and the muzzle launch stage.

The initial phase of the propulsion process can be modeled as the rising period of a pulsed magnetic field as the current in the armature increases from zero to a large value. The literature [55] tested the failure of various electronic components in this case. Experiments show that most of the devices work properly. The only exception is that floppy disks suffers from data loss and the miniature single-axis fluxgate magnetometer cannot work, as shown in Fig. 11b.

At the muzzle, the change in the magnetic field is more rapid. In literature [55], a coil is used to build a simulation experiment platform for this case and more device failure phenomena are found. For example, the lithium battery expands and a part of its internal filling leaks out; the light emitted by the laser diode contains white spots; the electronic components in the camera module are severely damaged and cannot work properly; and the DDR-2 RAM is severely affected by electrical shock, and some components fall off, as shown in Fig. 11c. In addition, memory cards, including Flash, SD, and USB; the on-board recorder (OBR) circuits, including FPGA, Hall sensor, the timer circuit; and the digital countdown timer may also experience different degrees of failure under the muzzle effect test.

3) FAILURE MECHANISM

The above failure phenomena can be explained from two aspects. First, the magnetic field during the process of propulsion is drastically changed, generating a high induced voltage. Under high voltage, breakdown may occur inside these electronic components. Moreover, the induced voltage causes internal violent heat generation of some resistive components, causing irreversible damage. The relationship between induced voltage and magnetic field change is

$$V = A\frac{dB}{dt} \tag{19}$$

where A represents the area of the device.

Second, some device failure is due to the magnetic pressure generated by a strong magnetic field [56], which is defined as

$$p = \frac{B^2}{2\mu_0} \tag{20}$$

where μ_0 is the magnetic permeability of vacuum.

Taking the test environment in the literature [55] as an example, consider the failure effect of the induced electric field: the change of the magnetic field with time in the initial stage of propulsion is $\frac{dB}{dt} \approx 19T/ms$, and at the moment of the muzzle, it exceeded 300 T/ms. Calculated by the area of the component A $=$ 1 cm^2, the induced voltage during the propulsion process is 1.9 V, and at the muzzle, it reaches more than 30 V. Consider the failure effect caused by the magnetic pressure effect: in the initial stage of propulsion, the magnetic field strength is 4.1 T, and the magnetic pressure is approximately p $=$ 7 MPa, which is still lower than the yield strength of most electronic component materials. At the muzzle, when the magnetic field strength reaches 10 T, the magnetic pressure reaches 40 MPa, which is much higher than the yield strength of most nonmetallic materials and light alloys. Therefore, under the muzzle effect test, more electronic devices fail, which poses a huge threat to the reliability of the electromagnetic railgun fuze.

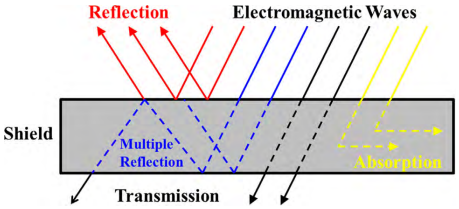

FIGURE 12. Mechanisms of EMI shielding [57].

B. ELECTROMAGNETIC SHIELDING TECHNOLOGY FOR ELECTROMAGNETIC RAILGUN FUZE

There are mainly three approaches for electromagnetic shielding, namely, reflection (R), absorption (A) and multiple reflection (B), as shown in Fig. 12 [57]. Reflections occur primarily in materials with highly conductive structures, such as metals and carbon materials that are widely used for electromagnetic shielding. Absorption requires that the electric and magnetic dipoles interact with the electromagnetic field in the radiation, for example, soft magnetic alloy powder and fiber joined in a polymer matrix. Multiple reflections occur at the surface or interface of the shielding material, requiring the shielding material to have a large surface area or interface area.

Electromagnetic shielding effectiveness (SE) is a combination of the above three effects, which is defined as follows [57]:

$$SE(dB) = R + A + B \tag{21}$$

$$R(dB) = 168 - 10\log(f\mu_r/\sigma_r) \tag{22}$$

$$A(dB) = 1.314t\sqrt{f\mu_r\sigma_r} \tag{23}$$

$$B(dB) = 20\log(1 - e^{-2t\sqrt{\pi\mu\sigma f}}) \tag{24}$$

where t is the shielding thickness, f is the frequency of electromagnetic radiation, μ is the magnetic permeability, σ is the electrical conductivity, σ_r is the electrical conductivity relative to copper, and μ_r is the relative magnetic permeability.

1) SHIELDING TECHNOLOGY BASED ON REFLECTION EFFECT

According to Eq. (22), to enhance the reflection effect, the shielding material needs to have a large electrical conductivity. Therefore, researchers conducted research on magnetic shielding materials based on highly conductive materials, such as metal materials, carbon materials, and so forth [57], [58]. For example, the work [57] studied a Mg-Z-Y-Zr alloy material. By controlling the ratio of Y, a second phase microstructure of honeycomb is stably formed, and it has superior scattering effects for the electromagnetic wave and can further enhance the electromagnetic shielding energy efficiency of the alloy material. As shown in Fig. 13a, which presents SEM micrographs of materials with increasing ratios of Y, from (1) to (5) corresponding to alloys 1-5. The corresponding electromagnetic shielding effectiveness is shown in Fig. 13b. It is found that the electromagnetic shielding effectiveness of the material is continuously improved, which

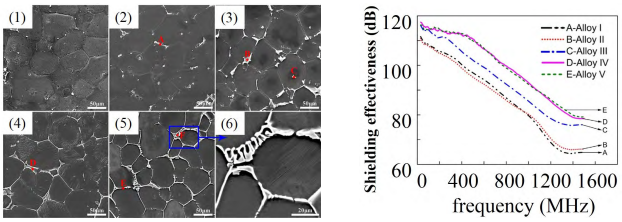

FIGURE 13. (a) SEM micrographs of the as-cast Mg-Zn-Zr-Y alloys: (1)-(5) alloys I - V, (6) SEM image showing the W-phase in alloy V [57]; (b) EMI shielding properties of the extruded Mg-Zn-Y-Zr alloys with different Y contents [57].

can exceed 110 dB at low frequencies and can reach 60 dB or higher in the high frequency region near 1.4 GHz. Considering the larger proportions of the low-frequency electromagnetic field during the launch process, it is effective for the protection of fuzes.

2) SHIELDING TECHNOLOGY BASED ON ABSORPTION EFFECT

According to Eq. (23), to enhance the absorption effect, the shielding material needs to have both a large electrical conductivity and a large magnetic permeability. Based on this principle, researchers studied electromagnetic shielding materials based on soft magnetic materials [59], [60]. The work [59] studied materials based on polyester fibers (PET) and stainless steel fibers (SSF). The paramagnetic austenite and ferromagnetic martensite crystalline phases of the soft magnetic 316L stainless steel fibers resulted in specific electrical and magnetic properties, which enabled the SSF/PET fabric to have a dielectric property, enhancing the absorption effect of the material, as shown in Fig. 14. The EMI SE of the material based on 100% SSF can be larger than 50 dB within the frequency of 0-1500 MHz, and the shielding effectiveness is obtained mainly from absorptivity, as large as more than 60%, and reflectivity. In particular, the EMI SE can be larger than 60 dB within 200 MHz, which is more conducive to the shielding during the launch process with larger proportions of the low-frequency electromagnetic field.

3) SHIELDING TECHNOLOGY BASED ON ABSORPTION AND REFLECTION EFFECTS

To further improve the electromagnetic shielding performance, recent research has proposed that through special nanostructure design, the material can simultaneously have both good absorption and good reflection, achieving effective electromagnetic shielding. The work [61] studied a low-density, ultrathin, flexible shielding material based on Fe_3O_4/graphene nanosheet (GN) papers. The schematic diagram of the magnetic shielding is shown in Fig. 15a. Microscopically, the triiron tetroxide particles are embedded in the graphene network. With the good electrical conductivity of graphene, the interface between the air and the air produces a good reflection effect, and a large proportion of the electromagnetic wave is directly reflected. After the remaining electromagnetic waves enter the interior of the composite,

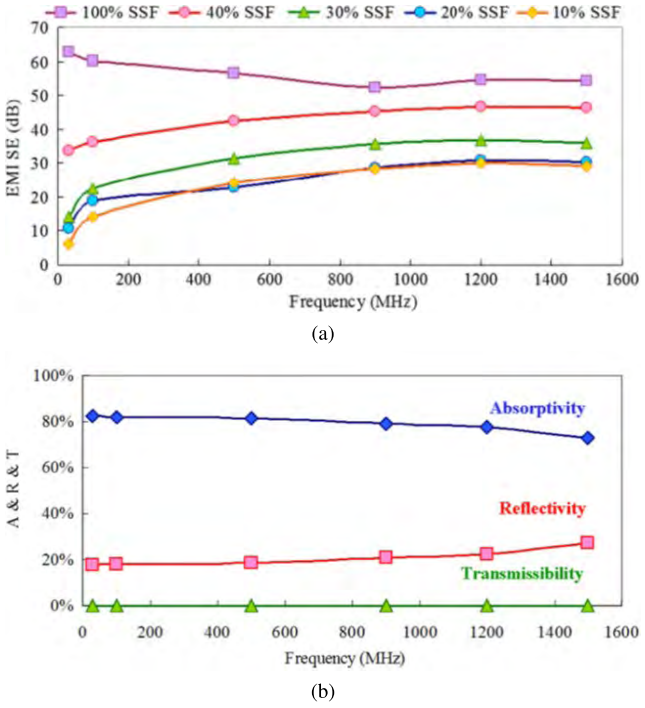

FIGURE 14. (a) The EMI SE of the fabrics as a function of frequency. (b) Ratio of reflectivity, absorptivity and transmissibility of SSF fabric as a function of frequency [59].

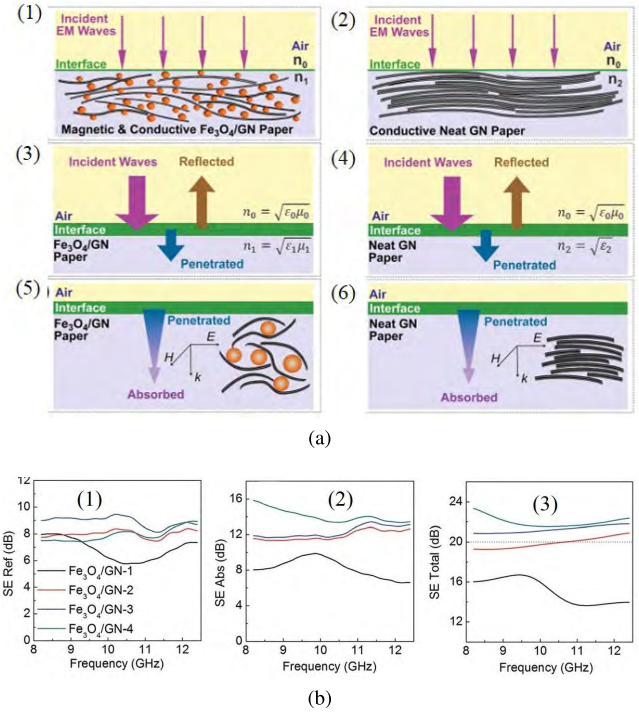

FIGURE 15. (a) Schematic diagram of magnetic shielding. (1) Schemes of the propagation of electromagnetic waves when they meet the neat GN. (2) Schemes of the propagation of electromagnetic waves when they meet the Fe_3O_4/GN papers. (3) Reflection at the surface of the neat GN paper. (4) Absorption in the Fe_3O_4/GN paper. (5) Reflection at surface of the neat GN paper. (6) Absorption in neat GN paper. [61]. (b) Shielding performance of the Fe_3O_4/GN papers with change of frequency. (1) SE_{ref} (2) SE_{abs} (3) total shielding effectiveness [61].

on the one hand, the graphene network with good electrical conductivity provides many paths for the generation of leakage current, converting more transmitted wave energy into heat energy. On the other hand, the magnetic dipole effect of ferroferric oxide also further consumes the energy of the incident electromagnetic waves. Finally, through the effect of the reflection and absorption, only a very small proportion of electromagnetic wave can pass through the shielding material, which provides a good shielding performance.

For the above composite material, the doping ratio of triiron tetroxide has a significant influence on its electromagnetic properties. By optimizing the doping ratio, the optimal magnetic shielding performance curve is obtained, as shown in Fig. 15b, and its electromagnetic shielding effectiveness is more than 20 dB in the range of 8-12 GHz. Its thickness is only 0.3 mm, which is approximately 1/10 of the metal shielding material. Therefore, if the thickness is equivalent to that of the metal shielding material, the shielding effectiveness will far exceed 70-80 dB of the metal, and its weight is much smaller than that of the metal material. This will greatly benefit the miniaturization, weight reduction and even flexibility of the electromagnetic railgun fuze.

4) SHIELDING TECHNOLOGY BASED ON MULTIPLE REFLECTION MECHANISM

The micro-nano structure of the material has an important influence on the electromagnetic shielding effect. Through the special micro-interface structure, the electromagnetic wave can be repeatedly reflected and its shielding effect is considerably better than that of the traditional conductive material and magnetic conductive material [62]–[64]. Based on the multireflection mechanism, the study [62] proposed a sandwich composite based on a pure iron-iron aluminum alloy-pure iron material. As shown in Fig. 16a, iron and aluminum are sufficiently diffused and reacted by high-temperature and high-pressure annealing in a vacuum environment to form a rich nonmagnetic iron-aluminum alloy interlayer. The material's multiple reflection behavior of the Fe-Al gradient layer causes most of the electromagnetic wave energy to be reflected or lost, and excellent electromagnetic shielding performance is obtained. The electromagnetic shielding effectiveness reaches 70-80 dB in the wide frequency range of 30 kHz to 1.5 GHz, as shown in Fig. 16b. With the extension of the diffusion time in the material preparation process, the reaction of the iron-aluminum alloy interlayer is more sufficient, the multi-reflection effect of the micro-interface is more remarkable, and the electromagnetic shielding effectiveness is further increased, as shown in Fig. 16c.

C. FAILURE OF THE FUZE IN STRONG MECHANICAL IMPACT ENVIRONMENT

1) GENERAL ELECTRONIC DEVICES

Basic electronic devices and chips are essential for all fuze systems, but unfortunately, ordinary commercial electronic devices have many non-negligible reliability problems under the strong mechanical impact environment during the elec-

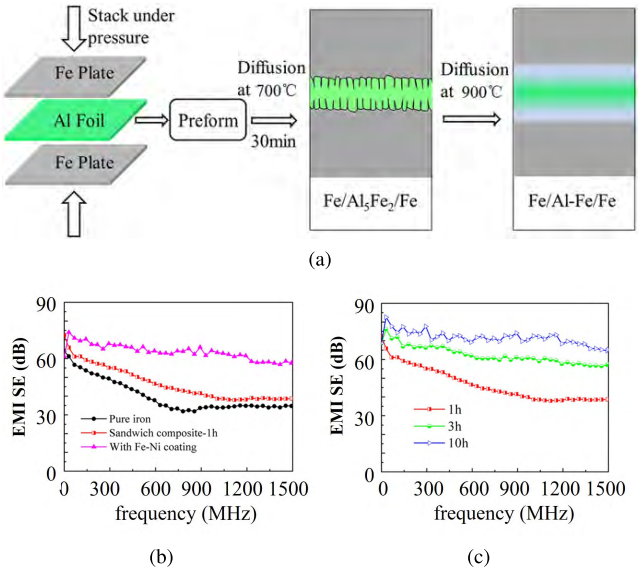

FIGURE 16. Schematic diagram of the fabrication process of the sandwich composite; (b) EMI shielding effectiveness of sandwich composites and pure iron plate; (c) EMI shielding effectiveness of sandwich composites with different diffusion times [62].

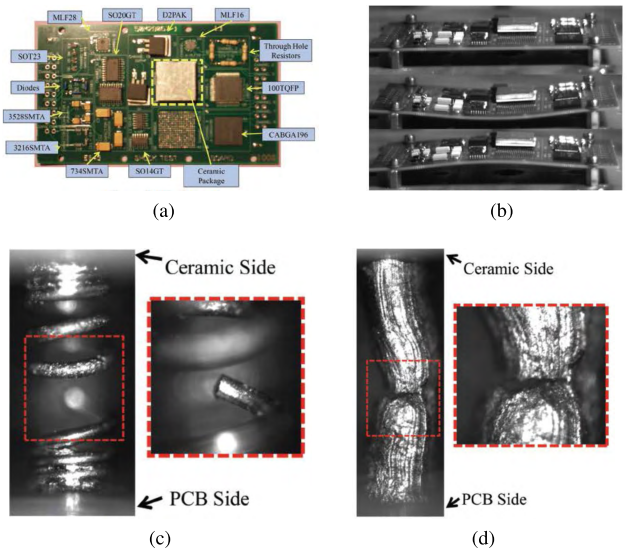

FIGURE 17. (a) Test board for high-*g* test; (b) undeformed, negative deflection, positive deflection during 1500 *g* test; (c) MCS failure mode; (d) CCGA failure mode [65].

tromagnetic railgun launch, threatening the stable operation of fuzes. The study [65] built a high-impact test platform of up to 50,000 *g* by a dual mass shock amplifier device, and they studied the failure phenomenon and mechanism of the circuit board composed of array electronic devices under high-*g* impact. The devices used for the testing are shown in Fig. 17a and consist of 14 types of 32 devices.

First, when experiencing an impact of 1500 *g*, a significant deformation of the circuit broad occurred, as shown in Fig. 17b. With such macroscopically significant large deformations, the package reliability of these arrayed electronic devices is unreliable.

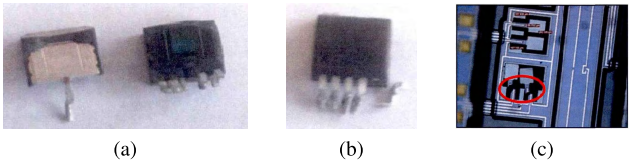

FIGURE 18. (a) The package damage of the sensor device under mechanical impact; (b) the pin breakage of the sensor device under mechanical impact; (c) the beam fracture of the sensor device under mechanical impact [66].

Through optical microscopy observations, the work [65] further studied the reliability of their high-*g* impact under the typical package structure of micro coil spring (MCS) and ceramic pillar grid array (CCGA), revealing their respective failure modes under mechanical impact. For MCS, there is the failure of the beryllium copper coil in the case of MCS interconnection. As shown in Fig. 17c, under high-*g* impact, the device suffers great shear stress, and thus, the coil produces axial stretching, compression, and shearing. For CCGA, the dominant effect is due to the excessive shear deformation of the intercolumn interconnect, resulting in failure of the intercolumn interconnection near the PCB interface, as shown in Fig. 17d.

The cause of the failure is the excessive stress and strain suffered by the package structure. The study [65] measures the stresses of the device under high-*g* impact of 1500 *g* and 50000 *g*, revealing the cause of the failure more clearly. The device encounters strong stress and strains with opposite directions, and the peak strains at the center point of the device reach 0.0033 and 0.0073, respectively, which is enough to cause irreversible damage to the material of the package structure.

2) SENSORS

Sensors such as accelerometers are the core components of the fuze to realize environment detection and target recognition, ensuring the safety and maximizing the effectiveness of the ammunition. The work [66] studied the failure of the sensors during the high-*g* impact process. The main failure phenomenon of the accelerometer with plastic packaging under mechanical impact is the package breakage of the sensor, as shown in Fig. 18a, and pin breakage and abnormal output signal, as shown in Fig. 18b. The main failure phenomenon of the accelerometer with the metal package under mechanical impact is the beam structure fracture, as shown in Fig. 18c. The high-frequency component in the mechanical impact causes the sensor structure to resonate and collide with the metal package outside the beam island domain, resulting in the fracture of the beam island structure.

D. ANTI-HIGH-G IMPACT TECHNOLOGY OF THE ELECTROMAGNETIC RAILGUN FUZE

To avoid failure of the electromagnetic railgun fuze under high-*g* impacts, anti-high-*g* impact technology of the electromagnetic railgun fuze has been widely studied from the device level, the system level and the integration level.

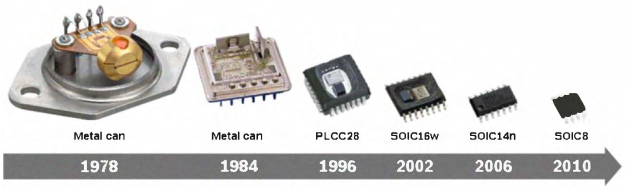

FIGURE 19. Package roadmap of automotive acceleration sensors [67].

First, for the various types of devices in the fuze, the smaller the volume of the device is, the smaller is the inertial force that it suffers at the same impact acceleration. Therefore, the miniaturization of key components in the fuze based on MEMS technology plays a fundamental role in enhancing the high-g impact reliability of fuzes. Second, for the design of the fuze system, the more devices that the system has, the more likely the system function is to fail due to the failure of a single device. The larger the total volume of each device is, the smaller is the volume that remains for the special anti-impact protection structure. Therefore, sensor components based on the self-powered principle help reduce the number and size of devices in the fuze system and enhance system reliability. Finally, at the integration level, the main method of impact protection is to add potting glue or buffer material as a protective structure on the outside of the device such that some impact can be properly filtered out and the force on the device can be reduced. After these three levels of protection, it can effectively reduce the interference and damage on the fuze under a high-g impact and ensure the normal operation of the fuze.

1) MEMS DEVICES FOR HIGH-G IMPACT APPLICATION

Under the inertial force of mechanical impact, there is a positive correlation between the stress in the device structure and the size of the device. Therefore, reducing the volume of the device helps to suppress the stress in the device structure under high-g impact and avoid mechanical failure. MEMS technology provides an effective technology to reduce the size of the sensor. For example, since the 1970s, high-g impact devices used in automotive safety systems have been continuously miniaturized through MEMS technology and successfully commercialized. Representative Bosch products in different generations and their processes are shown in Fig. 19 [67].

In the field of fuzes, extensive research has been conducted on various MEMS devices in high-g impact environments. The work [68], [69] studied a MEMS accelerometer with self-supporting piezoresistive microbeam structure, as shown in Fig. 20(a), with a sense range up to 100,000 g. An out-of-plane micro airflow sensor based on the hot-wire sensing principle is presented in [70]. The microsensors are fabricated on an out-of-plane Pyrex bubble with height of 300 μm, as shown in Fig. 20(b). An all-metal inertial microswitch is fabricated by low-temperature photoresist modeled metal-electroplating technology in [71]. To reduce

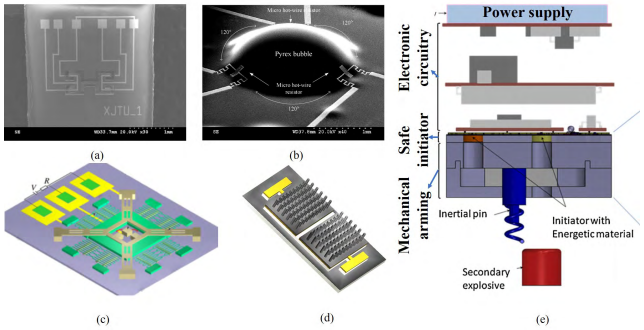

FIGURE 20. (a) SEM and output curve of high-g accelerometer [68], [69]; (b) SEM of the airflow sensor [70]; (c) the schematic diagram of triaxial inertial switch [71]; (d) MEMS-based power source [72]; (e) the MEMS SAF device made of three stacked parts: electronic circuitry, Si-based safe initiator and the mechanical arming function [73].

the cross-axis sensitivity and increase the axis sensitivity, a movable electrode suspended by a conjoined serpentine spring was designed, as shown in Fig. 20(c).

In addition to MEMS sensors, MEMS-based power sources have also been considerably developed [72], [74], [75], and the energy storage performance continues to improve. In [74], the electrodes are based on electrochemical polymerized polypyrrole (PPy) films, the electrolyte is based on NaCl, and a power density of 1.28 mW·cm^{-2} is achieved. In [72], through the MEMS 3D structure shown in Fig. 20(d), a capacitance density of 99.3 mF·cm^{-2} is achieved based on an electrode of tubular $RuO_2 \cdot xH_2O$ and electrolyte of Na_2SO_4.

Based on the MEMS device, microsystems have also been studied against high-g environments. For example, the Safe Arm and Fire (SAF) system is the core for the safety of ammunition, and a MEMS SAF device has been successfully developed [73]. The whole SAF system, including a mechanical arming unit and the electrical safety functionalities, is developed on one silicon initiator's chip, and the volume is only 1 cm^3. The structure and the operation procedure of the MEMS SAF device are shown in Fig. 20(e).

According to the literature [66], although the MEMS sensor has advantages over the traditional device in anti-high-g impacts, it is still possible to fail under extremely high-g impacts. To avoid this problem, there are currently two methods to further enhance the anti-high-g performance of MEMS devices. One is to optimize the design of the MEMS structure of the MEMS device; the other is to protect the MEMS sensor through a special package.

The work [76] studied a cantilever beam impact sensor, as shown in Fig. 21a. To avoid excessive deformation of the cantilever beam caused by excessive impact, the sensor is designed with a specially shaped frame in the direction of the cantilever beam deformation, as shown in Fig. 21b. When the deformation of the cantilever exceeds a certain range, no further deformation will occur due to the frame limitation. Thus, the sensor can measure the impact acceleration in the range and output the saturation signal without damage when the impact acceleration exceeds the range.

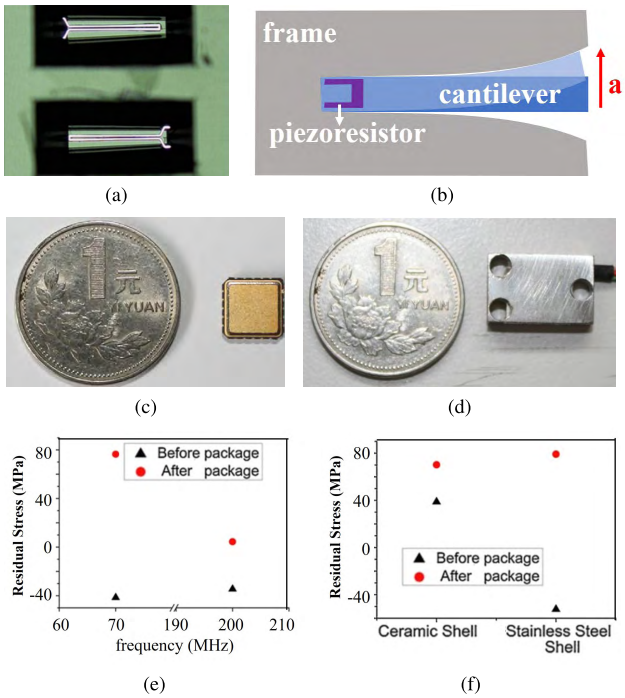

FIGURE 21. (a) Micrograph of a fabricated cantilever beam accelerometer; (b) sketch of the over-range stop curvature [76]; (c) packaged accelerometer with ceramic shell; (d) packaged accelerometer with stainless steel shell; (e) the residual stress variation before and after the package: effect of the die adhesive thickness on the accelerometer. (f) The residual stress variation before and after the package: effect of the package shell material on the accelerometer [77].

The work [77] studied the residual stress in the packages of the MEMS device, and its package is shown in Fig. 21c and Fig. 21d. The study reveals that the main cause of the large residual stress is the material mismatch between the package shell, the die bond and the MEMS structure. By using a thicker mold binder, the increase in residual stress can be significantly reduced. The study also examines the effects of encapsulating shell materials, noting that ceramic shells have superior anti-high-*g* performance compared to stainless steel shells. The test results are shown in Fig. 21e and Fig. 21f.

2) SELF-POWERED SENSORS FOR HIGH-*G* IMPACT APPLICATIONS

The power source and the connection between the power source and sensors are important destabilizing factors under a high-*g* impact. Self-powered sensors are an effective way to solve this problem. On the one hand, self-powered sensors do not require an additional power source, thus avoiding sensor failure due to power source failure. On the other hand, through the self-power supply of the sensor, the total power consumption of the fuze system can be reduced, thereby reducing the total volume of the system, and in the same situation, leaving more space to fill with buffer material.

Triboelectric nanogenerators (TENGs) have become a research hotspot in recent years, which realize the self-powering of the device through the tribo electrification

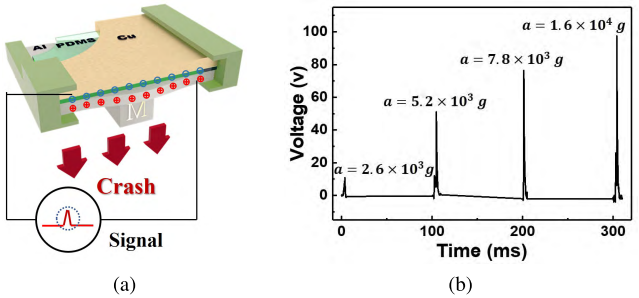

FIGURE 22. (a) Working diagram of the high-*g* sensor based on TENG; (b) output voltage under different high-*g* impacts [78].

effect without the need for an additional power source. A TENG was first applied for high-*g* impact sensing in [78]. As is shown in Fig. 22a, the device achieves impact sensing without an external power supply due to the deformation of the triboelectric layer under high-*g* impact. The amplitude of the voltage peak has a linear relation with the magnitude of the high-*g* impact, achieving accurate sensing, as shown in Fig. 22b. Moreover, the performance of the TENG-based high-*g* impact sensor is enhanced by optimizing the material [79].

Another method for self-powered sensor research is the integrated implementation of energy prestorage and sensing functions simultaneously through one porous electrode. The works [80]–[82] proposed a self-powered impact sensor based on a porous carbon material film. First, the work [80] found that the electrochemical capacitor based on a porous material electrode has a sensitive phenomenon of output voltage increase under high-*g* impact. For the first time, impact sensing up to 18000 *g* is realized, and the scheme of the device is shown in Fig. 23a and Fig. 23b. As shown in Fig. 23c, the output signal of the sensor under three short impacts and three long impacts has less clutter compared with the traditional mechanical sensor. For extreme high-*g* impact, the output voltage signal is a single peak with no clutter. Further theoretical research [81] explained this self-filtering phenomenon and discussed the advantage of the sensitive signal for impact identification.

In addition to self-powered accelerometers, there are various self-powered sensors and fundamental electronic devices based on TENG and other self-power mechanisms. A self-powered magnetic sensor is presented in [83], and the schematic diagram and the corresponding measurement setup are shown in Fig. 24a. A self-powered CMOS imager is presented in [84], and the cross-section of the proposed energy-harvesting pixel structure is shown in Fig. 24b. In [85], [86], two self-powered transistors based on TENG are presented. As shown in Fig. 24c, a self-powered nonvolatile ferroelectric transistor memory device is developed with the integration of the TENG device with a ferroelectric-gate field effect transistor. As shown in Fig. 24d, the flexible transparent tribotronic transistor (FTT) is based on an organic thin film transistor (OTFT) and a TENG in free-standing sliding mode [86]. These novel self-powered devices provide a new way to

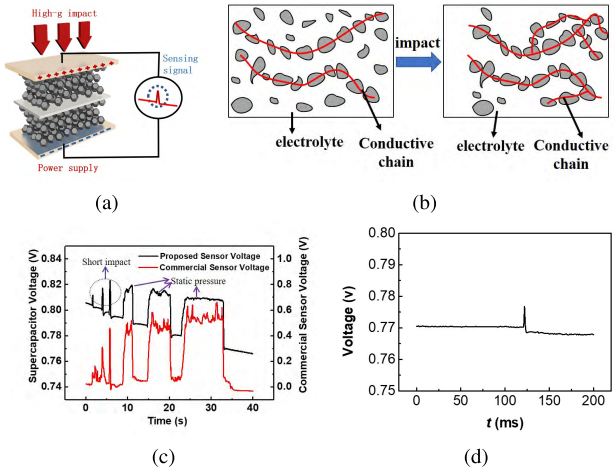

FIGURE 23. Self-powered sensor based on porous carbon. (a) The structure and mechanism of the sensor; (b) the increase in microconductive chains under high-*g* impact; (c) the sensing signal under short and long press; (d) sensing signal with no clutter under high-*g* impact. material [80]–[82].

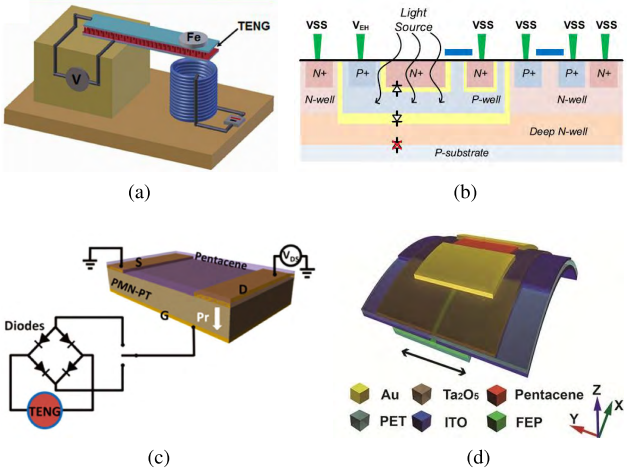

FIGURE 24. (a) Self-powered magnetic sensor [83]; (b) self-powered CMOS imager [84]; (c) self-powered transistor [85]; (d) self-powered transistor [86].

improve the performance of electromagnetic railgun fuzes under high-*g* impacts.

3) BUFFER MATERIAL FOR HIGH-*G* IMPACT ENVIRONMENT

The potting process is an effective method for protecting electronic devices from external environmental threats. The work [87] studied the protective effect of epoxy resin potting material and polyurethane sealing material on different postures of the circuit board, and the optimal attitude corresponding to different potting materials was determined by finite element simulation analysis. Fig. 25a and Fig. 25b show the equivalent stress simulation and stress of the epoxy potting structure board versus time. It is found that the board should be placed vertically to reduce the maximum stress that it experiences. The work [88] studied the influence of material properties, such as the Young's modulus of potting glue, on the distortion of the post-package acceleration sensor signal, and it analyzed the selection principle of potting material considering both impact stability and sensing signal accuracy.

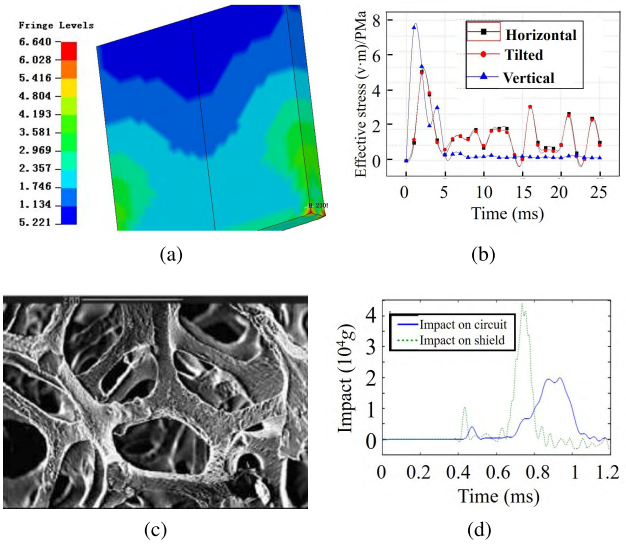

FIGURE 25. (a) Equivalent stress simulation of epoxy potting structure circuit board; (b) stress of the epoxy potting structure board versus time [87]; (c) microstructure of aluminum foam; (d) impact before and after the buffering protection [89].

Similar to the potting process, buffering protection is also an effective way to protect circuits from high-*g* impacts. In [89], aluminum foam is studied for buffering protection. The aluminum foam is based on the metal and alloy, with a large amount of air bubbles distributed inside, and it has dual properties of metal and porous structure. The microstructure is shown in Fig. 25c. On the one hand, the aluminum possesses excellent mechanical characteristics. Its compressive strength is comparable to that of eucalyptus and concrete foam, while the weight can even be lighter than water. On the other hand, it also has high energy absorption characteristics, including sound absorption, heat insulation, magnetic field shielding, and corrosion resistance. Moreover, it is nontoxic and volatile free.

The impact on the shield of the test equipment before and after the buffering protection is shown in Fig. 25d, where the maximum impact is decreased from 44000 *g* to 20000 *g*. It is verified that the maximum impact on the circuit module is significantly reduced.

V. CONCLUSION

In recent years, a large number of experimental and theoretical studies have been conducted on the harsh environment of the electromagnetic railgun launch process, such as strong magnetic field, high-*g* impact, high temperature, and so on. Such environments may lead to the failure of key components in the fuze, making the fuze lose the capability of target recognition and detonation control and threatening the reliability of the ammunition. These harsh environmental effects are also coupled to each other, and the interaction aggravates the extreme environment. This 'chain reaction'

makes it more important to protect the fuze during the launch of the electromagnetic railgun.

The protection of the fuzes in harsh environments mainly includes magnetic shielding and anti-high-*g* impact technology. The magnetic shielding is primarily based on the three effects of reflection, absorption and multiple reflection, as well as their combination. Through the study of advanced shielding materials, the shielding effectiveness can be larger than 110 dB at low frequencies. At present, with the achieved excellent shielding effectiveness, research is beginning to focus on ultrathin materials. Such materials will also help to reduce the total volume of fuzes, and it must be one of the trends of magnetic shielding for fuzes. The study on anti-high-*g* impact technology of fuzes is performed from three aspects: device, system and package. The research on the miniaturization of devices based on MEMS technology has been fully developed. Research for reducing the stress concentration inside the MEMS structure through special design and optimization of the microstructure has been conducted, but the effect still needs to be improved, which will be a trend in the future. Moreover, simplifying the system and reducing the total volume based on self-powered devices has turned out to be an effective anti-high-*g* impact technology. Applying developed self-powered sensors on the fuze may also help to promote its reliability. These research hotspots that are underway may provide new ways for the magnetic shielding and anti-high-*g* impact technology of the fuzes in practice, thus promoting the reliability of ammunition and increasing the damage effectiveness of electromagnetic guns.

REFERENCES

[1] A. C. Charters, "Development of the high-velocity gas-dynamics gun," *Int. J. Impact Eng.*, vol. 5, nos. 1–4, pp. 181–203, 1987.

[2] N. Doerry, J. Amy, and C. Krolick, "History and the status of electric ship propulsion, integrated power systems, and future trends in the U.S. Navy," *Proc. IEEE*, vol. 103, no. 12, pp. 2243–2251, Dec. 2015.

[3] W. Ma and J. Lu, "Electromagnetic launch technology," (in Chinese), *J. Nat. Univ. Defense Technol.*, vol. 38, no. 6, pp. 1–5, 2016.

[4] X. Liu, X. Yu, and X. Liu, "Performance analysis and parameter optimization of CPPS-based electromagnetic railgun system," *IEEE Trans. Plasma Sci.*, vol. 44, no. 3, pp. 281–288, Mar. 2016.

[5] J. McFarland and I. R. McNab, "A long-range naval railgun," *IEEE Trans. Magn.*, vol. 39, no. 1, pp. 289–294, Jan. 2003.

[6] I. R. McNab, "Early electric gun research," *IEEE Trans. Magn.*, vol. 35, no. 1, pp. 250–261, Jan. 1999.

[7] O. Liebfried, "Review of inductive pulsed power generators for railguns," *IEEE Trans. Plasma Sci.*, vol. 45, no. 7, pp. 1108–1114, Jul. 2017.

[8] A. Sitzman, D. Surls, and J. Mallick, "Design, construction, and testing of an inductive pulsed-power supply for a small railgun," *IEEE Trans. Magn.*, vol. 43, no. 1, pp. 270–274, Jan. 2007.

[9] A. Sitzman, D. Surls, and J. Mallick, "Modification and testing of a battery-inductor repetitive pulsed power supply for a small railgun," in *Proc. 16th IEEE Int. Pulsed Power Conf.*, vol. 2, Jun. 2007, pp. 1793–1798.

[10] J. Dong, J. Zhang, J. Li, and N. Su, "The 100-kJ modular pulsed power units for railgun," *IEEE Trans. Plasma Sci.*, vol. 39, no. 1, pp. 275–278, Jan. 2011.

[11] D. Hackworth, D. Deis, P. Eckels, and D. Marschik, "A 10 MJ cryogenic inductor," *IEEE Trans. Magn.*, vol. 22, no. 6, pp. 1495–1498, Nov. 1986.

[12] O. Liebfried and V. Brommer, "A four-stage XRAM generator as inductive pulsed power supply for a small-caliber Railgun," *IEEE Trans. Plasma Sci.*, vol. 41, no. 10, pp. 2805–2809, Oct. 2013.

[13] H. D. Fair, "Electromagnetic launch: A review of the U.S. national program," *IEEE Trans. Magn.*, vol. 33, no. 1, pp. 11–16, Jan. 1997.

[14] A. Brooks, R. Hawke, J. Scudder, and C. Wozynski, "Design and fabrication of large-and small-bore railguns," *IEEE Trans. Magn.*, vol. MAG-18, no. 1, pp. 68–81, Jan. 1982.

[15] D. Deis, D. Scherbarth, and G. Ferrentino, "Emack electromagnetic launcher commissioning," *IEEE Trans. Magn.*, vol. MAG-20, no. 2, pp. 245–248, Mar. 1984.

[16] R. J. Hayes and R. C. Zowarka, Jr., "Experimental results from CEM-UT's single shot 9 MJ railgun," *IEEE Trans. Magn.*, vol. 27, no. 1, pp. 33–38, Jan. 1991.

[17] I. R. McNab, F. LeVine, and M. Aponte, "Experiments with the Green Farm electric gun facility," *IEEE Trans. Magn.*, vol. 31, no. 1, pp. 338–343, Jan. 1995.

[18] H. D. Fair, "Electromagnetic launch science and technology in the United States enters a new era," *IEEE Trans. Magn.*, vol. 41, no. 1, pp. 158–164, Jan. 2005.

[19] J. V. Parker, D. T. Berry, and P. T. Snowden, "The IAT electromagnetic launch research facility," *IEEE Trans. Magn.*, vol. 33, no. 1, pp. 129–133, Jan. 1997.

[20] H. D. Fair, "Progress in electromagnetic launch science and technology," *IEEE Trans. Magn.*, vol. 43, no. 1, pp. 93–98, Jan. 2007.

[21] M. Crawford *et al.*, "The design and testing of a large-caliber railgun," in *Proc. 14th Symp. Electromagn. Launch Technol.*, Jun. 2008, pp. 1–5.

[22] W. A. Walls, W. F. Weldon, S. B. Pratap, M. Palmer, and D. Adams, "Application of electromagnetic guns to future naval platforms," *IEEE Trans. Magn.*, vol. 35, no. 1, pp. 262–267, Jan. 1999.

[23] J. Hogg, "Keynote address: History of the U.S. navy railgun program," *IEEE Trans. Plasma Sci.*, vol. 45, no. 7, pp. 1069–1070, Jul. 2017.

[24] I. R. McNab *et al.*, "Development of a naval railgun," *IEEE Trans. Magn.*, vol. 41, no. 1, pp. 206–210, Jan. 2005.

[25] I. R. McNab and F. C. Beach, "Naval railguns," *IEEE Trans. Magn.*, vol. 43, no. 1, pp. 463–468, Jan. 2007.

[26] *F. G. Navy Sets New World Record With Electromagnetic Railgun Demonstration*. Accessed: Jan. 29, 2018. [Online]. Available: http://www.navy.mil/submit/display.asp?story_id=57690

[27] DoD. *Electromagnetic Railgun Firing Test at Dahlgren Range*. Accessed: Jan. 29, 2018. [Online]. Available: https://www.youtube.com/watch?v=fTjj-DhtgYo

[28] J.-H. Jeong *et al.*, "Miniature mechanical safety and arming device with runaway escapement arming delay mechanism for artillery fuze," *Sens. Actuators A, Phys.*, vol. 279, pp. 518–524, Aug. 2018.

[29] C. Song, K. Wang, and L. Zheng, "The image processing and target identification of laser imaging fuze," in *Proc. 3rd Int. Conf. Intell. Syst. Knowl. Eng.*, vol. 1, Nov. 2008, pp. 1117–1120.

[30] A. Nasser, F. M. Ahmed, K. H. Moustafa, and A. Elshabrawy, "Recent advancements in proximity fuzes technology," *Int. J. Eng. Res. Technol.*, vol. 4, no. 4, pp. 1–7, 2015.

[31] B. Schwartz, F. Herr, and R. Bryan, "Fuzing for use in an electromagnetic gun," in *Proc. 49th Annu. Fuze Conf.*, 2005, pp. 1–18.

[32] B. Schwartz and D. Okken, "A novel fuze for use in an EM gun projectile," in *Proc. 50th Annu. Fuze Conf.*, 2006, pp. 1–19.

[33] D. Motes, J. Keena, K. Womack, F. Stefani, and M. Crawford, "Thermal analysis of high-energy railgun tests," *IEEE Trans. Plasma Sci.*, vol. 40, no. 1, pp. 124–130, Jan. 2012.

[34] S. Hundertmark, M. Schneider, and G. Vincent, "Payload acceleration using a 10-MJ des railgun," *IEEE Trans. Plasma Sci.*, vol. 41, no. 5, pp. 1455–1459, May 2013.

[35] R. Cao, J. Li, Q. Jiao, and J. Yuan, "Measure variation of magnetic field waveforms above the rails of rail-gun during the launching period," in *Proc. 16th Int. Symp. Electromagn. Launch Technol.*, May 2012, pp. 1–4.

[36] Q. Li, M. Wei, Q.-A. Lv, H. Xiang, and B. Lei, "Simulation on controlled strong magnetic environment for electronic fuze during railguns launching," in *Proc. 3rd Int. Conf. Inf. Sci. Control Eng. (ICISCE)*, Jul. 2016, pp. 1121–1125.

[37] T. Stankevic, M. Schneider, and S. Balevičius, "Magnetic diffusion inside the rails of an electromagnetic launcher: Experimental and numerical studies," *IEEE Trans. Plasma Sci.*, vol. 41, no. 10, pp. 2790–2795, Oct. 2013.

[38] T. Stankevič *et al.*, "Pulsed magnetic field measurement system based on colossal magnetoresistance-B-scalar sensors for railgun investigation," *Rev. Sci. Instrum.*, vol. 85, Apr. 2014, Art. no. 044704.

[39] M. Ghassemi and R. Pasandeh, "Thermal and electromagnetic analysis of an electromagnetic launcher," *IEEE Trans. Magn.*, vol. 39, no. 3, pp. 1819–1822, May 2003.

[40] M. Schneider, M. Woetzel, W. Wenning, and D. Walch, "The ISL rapid fire railgun project RAFIRA part I: Technical aspects and design considerations," *IEEE Trans. Magn.*, vol. 45, no. 1, pp. 442–447, Jan. 2009.
[41] S. Song and C. Cheng, "Measurement of solid armature's in-bore velocity using b-dot probes in a series-augmented railguns," *IEEE Trans. Plasma Sci.*, vol. 43, no. 5, pp. 1310–1315, May 2015.
[42] S. Myers and R. Zapata-Ramos, "Application of W-band, Doppler radar to railgun velocity measurements," *Procedia Eng.*, vol. 58, pp. 369–376, 2013.
[43] Y.-H. Lee, S.-H. Kim, B.-H. Lee, S. An, and K.-S. Yang, "Experimental tests of a 25 mm square-bore railgun," in *Proc. 16th Int. Symp. Electromagn. Launch Technol.*, May 2012, pp. 1–6.
[44] W. Zhi-Heng, W. Min, and L. Xiao-Jiang, "Numerical modeling of electromagnetic railgun rail temperature field," *Int. J. Appl. Electromagn. Mech.*, vol. 51, no. 2, pp. 173–183, Jun. 2016.
[45] Q.-H. Lin and B.-M. Li, "Numerical simulation of interior ballistic process of railgun based on the multi-field coupled model," *Defence Technol.*, vol. 12, no. 2, pp. 101–105, Apr. 2016.
[46] J. D. Powell and A. E. Zielinski, "Observation and simulation of solid-armature railgun performance," *IEEE Trans. Magn.*, vol. 35, no. 1, pp. 84–89, Jan. 1999.
[47] X. Feng, M. Ouyang, X. Liu, L. Lu, Y. Xia, and X. He, "Thermal runaway mechanism of lithium ion battery for electric vehicles: A review," *Energy Storage Mater.*, vol. 10, pp. 246–267, Jan. 2018.
[48] J.-G. Wu, B. Tang, Q.-H. Lin, H.-Y. Li, and B.-M. Li, "3D numerical simulation and analysis of railgun gouging mechanism," *Defence Technol.*, vol. 12, no. 2, pp. 90–95, 2016.
[49] S. Bair *et al.*, "A survey of railgun research at the georgia institute of technology (USA)," in *Proc. 16th Int. Symp. Electromagn. Launch Technol.*, May 2012, pp. 1–6.
[50] G. R. Johnson, "A constitutive model and data for materials subjected to large strains, high strain rates, and high temperatures," in *Proc. 7th Inf. Symp. Ballistics*, 1983, pp. 541–547.
[51] B. Tang, Y. Xu, Q. Lin, and B. Li, "Synergy of melt-wave and electromagnetic force on the transition mechanism in electromagnetic launch," *IEEE Trans. Plasma Sci.*, vol. 45, no. 7, pp. 1361–1367, Jul. 2017.
[52] Q. Yin, H. Zhang, H.-J. Li, and Y.-X. Yang, "Analysis of in-bore magnetic field in C-shaped armature railguns," *Defence Technol.*, vol. 15, pp. 83–88, Feb. 2019.
[53] B. Tang, Q. Lin, and B. Li, "Research on thermal stress by current skin effect in a railgun," *IEEE Trans. Plasma Sci.*, vol. 45, no. 7, pp. 1689–1694, Jul. 2017.
[54] L. Tang, "Analysis of electromagnetic railgun projectile fuze's high magnetic field environment and its shield design and utilization," M.S. thesis, School Mech. Eng., Nanjing Univ. Sci. Technol., Nanjing, Xuanwu, 2014.
[55] R. Ciolini, M. Schneider, and B. Tellini, "The use of electronic components in railgun projectiles," in *Proc. 14th Symp. Electromagn. Launch Technol.*, Jun. 2008, pp. 1–6.
[56] H. Knoepfel, *Pulsed High Magnetic Fields: Physical Effects and Generation Methods Concerning Pulsed Fields Up to the Megaoersted Level*. Amsterdam, The Netherlands: North-Holland, 1970.
[57] X. Chen, L. Liu, J. Liu, and F. Pan, "Microstructure, electromagnetic shielding effectiveness and mechanical properties of Mg–Zn–Y–Zr alloys," *Mater. Design*, vol. 65, pp. 360–369, Jan. 2015.
[58] X. Chen, L. Liu, F. Pan, J. Mao, X. Xu, and T. Yan, "Microstructure, electromagnetic shielding effectiveness and mechanical properties of Mg–Zn–Cu–Zr alloys," *Mater. Sci. Eng., B*, vol. 197, pp. 67–74, Jul. 2015.
[59] T.-W. Shyr and J.-W. Shie, "Electromagnetic shielding mechanisms using soft magnetic stainless steel fiber enabled polyester textiles," *J. Magn. Magn. Mater.*, vol. 324, no. 23, pp. 4127–4132, 2012.
[60] S. W. Kim *et al.*, "Electromagnetic shielding properties of soft magnetic powder–polymer composite films for the application to suppress noise in the radio frequency range," *J. Magn. Magn. Mater.*, vol. 316, no. 2, pp. 472–474, 2007.
[61] W.-L. Song *et al.*, "Magnetic and conductive graphene papers toward thin layers of effective electromagnetic shielding," *J. Mater. Chem. A*, vol. 3, no. 5, pp. 2097–2107, 2015.
[62] X. Ma, Q. Zhang, Z. Luo, X. Lin, and G. Wu, "A novel structure of Ferro-Aluminum based sandwich composite for magnetic and electromagnetic interference shielding," *Mater. Des.*, vol. 89, pp. 71–77, Jan. 2016.
[63] G. Wu, X. Huang, Z. Dou, S. Chen, and L. Jiang, "Electromagnetic interfering shielding of aluminum alloy–cenospheres composite," *J. Mater. Sci.*, vol. 42, no. 8, pp. 2633–2636, 2007.
[64] Z. Dou, G. Wu, X. Huang, D. Sun, and L. Jiang, "Electromagnetic shielding effectiveness of aluminum alloy–fly ash composites," *Compos. A, Appl. Sci. Manuf.*, vol. 38, no. 1, pp. 186–191, 2007.
[65] P. Lall *et al.*, "Modeling and reliability characterization of area-array electronics subjected to high-g mechanical shock up to 50,000 g," in *Proc. IEEE 62nd Electron. Compon. Technol. Conf.*, May/Jun. 2012, pp. 1194–1204.
[66] B. Liu, "Failure analysis of acceleration sensor under high-g impact," M.S. thesis, Inst. Electron. Eng., China Acad. Eng. Phys., Mianyang, China, 2017.
[67] J. Marek, "Trends and challenges in modern MEMS sensor packages," in *Proc. Symp. Design, Test, Integr. Packag. MEMS/MOEMS (DTIP)*, May 2011, pp. 1–3.
[68] Y. Zhao, X. Li, L. Jing, and Z. Jiang, "Design, fabrication and experiment of a MEMS piezoresistive high-g accelerometer," *J. Mech. Sci. Technol.*, vol. 27, no. 3, pp. 831–836, 2013.
[69] C. Jia *et al.*, "Impact experiment analysis of MEMS ultra-high g piezoresistive shock accelerometer," in *Proc. IEEE Int. Conf. Micro Electro Mech. Syst. (MEMS)*, Jan. 2018, pp. 964–967.
[70] S. Liu *et al.*, "Out-of-plane micro triple-hot-wire anemometer based on pyrex bubble for airflow sensing," in *Proc. IEEE 27th Int. Conf. Micro Electro Mech. Syst. (MEMS)*, Jan. 2014, pp. 777–780.
[71] W. Chen, Y. Wang, G. Ding, H. Wang, X. Zhao, and Z. Yang, "Simulation, fabrication and characterization of an all-metal contact-enhanced triaxial inertial microswitch with low axial disturbance," *Sens. Actuators A, Phys.*, vol. 220, pp. 194–203, Dec. 2014.
[72] X. Wang, Y. Yin, X. Li, and Z. You, "Fabrication of a symmetric micro supercapacitor based on tubular ruthenium oxide on silicon 3D microstructures," *J. Power Sources*, vol. 252, pp. 64–72, Apr. 2014.
[73] H. Pezous *et al.*, "Integration of a MEMS based safe arm and fire device," *Sens. Actuators A, Phys.*, vol. 159, no. 2, pp. 157–167, 2010.
[74] W. Sun, R. Zheng, and X. Chen, "Symmetric redox supercapacitor based on micro-fabrication with three-dimensional polypyrrole electrodes," *J. Power Sources*, vol. 195, no. 20, pp. 7120–7125, 2010.
[75] W. Yang *et al.*, "Carbon-MEMS-based alternating stacked MoS_2@rGO-CNT micro-supercapacitor with high capacitance and energy density," *small*, vol. 13, no. 26, 2017, Art. no. 1700639.
[76] J. Dong, X. Li, Y. Wang, D. Lu, and S. Ahat, "Silicon micromachined high-shock accelerometers with a curved-surface-application structure for over-range stop protection and free-mode-resonance depression," *J. Micromech. Microeng.*, vol. 12, no. 6, pp. 742–746, Aug. 2002.
[77] J. Liu, Y. Shi, P. Li, J. Tang, R. Zhao, and H. Zhang, "Experimental study on the package of high-g accelerometer," *Sens. Actuators A, Phys.*, vol. 173, no. 1, pp. 1–8, 2012.
[78] K. Dai, X. Wang, F. Yi, C. Jiang, R. Li, and Z. You, "Triboelectric nanogenerators as self-powered acceleration sensor under high-g impact," *Nano Energy*, vol. 45, pp. 84–93, Mar. 2018.
[79] C. Garciaa, I. Trendafilova, and J. S. del Rio, "Detection and measurement of impacts in composite structures using a self-powered triboelectric sensor," *Nano Energy*, vol. 56, pp. 443–453, Feb. 2019.
[80] K. Dai *et al.*, "Discharge voltage behavior of electric double-layer capacitors during high-g impact and their application to autonomously sensing high-g accelerometers," *Nano Res.*, vol. 11, no. 2, pp. 1146–1156, 2018.
[81] K. Dai, X. Wang, R. Li, H. Zhang, and Z. You, "Theoretical study and applications of self-sensing supercapacitors under extreme mechanical effects," *Extreme Mech. Lett.*, vol. 26, pp. 53–60, Jan. 2019.
[82] K. Dai, X. Wang, Z. You, and H. Zhang, "Pressure sensitivity enhancement of porous carbon electrode and its application in self-powered mechanical sensors," *Micromachines*, vol. 10, no. 1, p. 58, 2019.
[83] Y. Yang, L. Lin, Y. Zhang, Q. Jing, T.-C. Hou, and Z. L. Wang, "Self-powered magnetic sensor based on a triboelectric nanogenerator," *ACS Nano*, vol. 6, no. 11, pp. 10378–10383, 2012.
[84] A. Y.-C. Chiou and C.-C. Hsieh, "A 137 dB dynamic range and 0.32 V self-powered CMOS imager with energy harvesting pixels," *IEEE J. Solid-State Circuits*, vol. 51, no. 11, pp. 2769–2776, Nov. 2016.
[85] H. Fang *et al.*, "A high performance triboelectric nanogenerator for self-powered non-volatile ferroelectric transistor memory," *Nanoscale*, vol. 7, no. 41, pp. 17306–17311, 2015.
[86] Y. Pang *et al.*, "Flexible transparent tribotronic transistor for active modulation of conventional electronics," *Nano Energy*, vol. 31, pp. 533–540, Jan. 2017.
[87] C. Zheng, "The research on shock resistance of circuit board and typical devices in different fuze potting structure," M.S. thesis, School Mech. Elect. Eng., North Univ. China, Taiyuan, China, 2015.

[88] W. Huang, X. Cai, B. Xu, L. Luo, X. Li, and Z. Cheng, "Packaging effects on the performances of MEMS for high-g accelerometer with double-cantilevers," *Sens. Actuators A, Phys.*, vol. 102, no. 3, pp. 268–278, 2003.
[89] J. Lu, "High overload buffer protection of light circuit module," M.S. thesis, Dept. Mech., North Univ. China, Taiyuan, China, 2016.

HE ZHANG was born in Henan, China. He received the Ph.D. degree in measurement technology and instruments from the Nanjing University of Aeronautics and Astronautics, Nanjing, China. He is currently a Professor with the School of Mechanical Engineering, Nanjing University of Science and Technology (NJUST), Nanjing. He is the Director of the Institute of Mechanical and Electrical Engineering, NJUST, where he is also the Associate Director of the ZNDY of Ministerial Key Laboratory. His research interests include mechatronics and weapon system applications. He is on the Editorial Board of the journal of *Detection and Control*.

KEREN DAI received the B.E. and Ph.D. degrees from Tsinghua University, Beijing, China, in 2014 and 2018, respectively. He is currently an Assistant Professor with the School of Mechanical Engineering, Nanjing University of Science and Technology. His research interests include system modeling and simulation, signal processing, power management systems, and micro power devices.

QIANG YIN was born in Jiangxi, China. He is currently pursuing the Ph.D. degree with the ZNDY of Ministerial Key Laboratory, Nanjing University of Science and Technology. His current research interests include electromagnetic launch technology and intelligent ammunition fuze technology.